

Effect of Selective Laser Melting on Microstructure, Mechanical, and Corrosion Properties of Biodegradable FeMnCS for Implant Applications

Julia Hufenbach,* Jan Sander, Fabian Kochta, Stefan Pilz, Andrea Voss, Uta Kühn, and Annett Gebert

Selective laser melting (SLM) of biodegradable metallic materials offers a great potential for manufacturing customized implants. Herein, SLM processing of a novel Fe–30Mn–1C–0.02S twinning-induced plasticity (TWIP) alloy and the resulting structural, mechanical, and corrosion properties are presented. The occurring rapid solidification results in a fine-grained austenitic microstructure with mainly homogeneous element distribution, which is investigated by scanning electron microscopy (SEM) combined with energy-dispersive X-ray spectroscopy (EDX) and electron backscatter diffraction (EBSD) as well as X-ray diffraction (XRD). By processing the alloy via SLM, significantly higher strengths under tensile and compressive load in comparison with those for the as-cast counterpart and a 316L reference steel are achieved. Electrochemical corrosion tests in a simulated body fluid (SBF) indicate a moderate corrosion activity, and a beneficial uniform degradation is shown in immersion tests in SBF. Regarding the envisaged application for vascular implants, SLM-processed stent prototypes out of the novel alloy are presented and a first functionality test is shown.

1. Introduction

Currently, additive manufacturing, e.g., selective laser melting (SLM), of biodegradable metals and alloys for implant applications is drawing increasing attention.^[1–5] This new class of materials is of highest interest as it enables progressive implant degradation after providing temporary support on the healing processes of the diseased tissue. So, revision surgery, chronic

inflammation, or lacking adaptation to growth (regarding diseases at infancy) can be avoided.^[6–8]

Among the biodegradable alloys, Fe-based systems, especially those on FeMn base, are very promising, e.g., for cardiovascular applications due to their excellent processability, a broad range of tunable mechanical properties, their high integrity during degradation, as well as degradation reactions without hydrogen gas evolution in physiological media. This was reported for a variety of alloy systems prepared by different casting and forming technologies.^[7–16] Especially, FeMnC-base alloys are promising candidates due to their higher strength and improved cell compatibility compared with many FeMn systems.^[11–15] This work is based on a novel developed FeMnCS alloy, which already shows an attractive combination of mechanical properties under tensile load, corrosion rate, and cell compatibility in the as-cast state, as shown in previous studies.^[11,14]

However, there are still challenges regarding a more homogeneous degradation for good temporary structural integrity, an adequate corrosion rate, as well as improved mechanical properties which are comparable or better than those of clinically applied 316L benchmark steel.

Until now, there are only a few published studies on the processing of biodegradable Mg-, Zn-, or Fe-based alloys by means of SLM.^[1–4,17–20] However, the layer-by-layer technique offers a flexible production of parts with a high degree of individualization or complex geometries and a high level of function integration, which can often not be generated by conventional manufacturing techniques.^[21,22] Furthermore, SLM is a rapid solidification technique, which yields particular microstructural phenomena like grain refinement, extended solid solubility and reduction of quantity, and size of phase segregations.

These effects can be very beneficial for the properties of metallic biomaterials as it was already demonstrated by different authors for various nondegradable materials like 316L, Ti-based, or CoCr-based alloys, also partially considering the influence of the SLM building orientation.^[21–29] Consequently, the exploitation of advantages of SLM for the production of patient-specific degradable implants with tailored microstructures appears to be a promising approach.

Prof. J. Hufenbach, Dr. J. Sander, F. Kochta, Dr. S. Pilz, A. Voss, Dr. U. Kühn, Dr. A. Gebert
Institute for Complex Materials
Leibniz IFW Dresden
Helmholtzstr. 20, 01069 Dresden, Germany
E-mail: j.k.hufenbach@ifw-dresden.de

Prof. J. Hufenbach
Institute of Materials Science
TU Bergakademie Freiberg
Gustav-Zeuner-Str. 5, 09599 Freiberg, Germany

 The ORCID identification number(s) for the author(s) of this article can be found under <https://doi.org/10.1002/adem.202000182>.

© 2020 The Authors. Published by WILEY-VCH Verlag GmbH & Co. KGaA, Weinheim. This is an open access article under the terms of the Creative Commons Attribution License, which permits use, distribution and reproduction in any medium, provided the original work is properly cited.

DOI: 10.1002/adem.202000182

In this work, the successful SLM processing of a novel Fe–30Mn–1C–0.02S alloy is demonstrated, and the consequences of high solidification rates for the microstructure, the mechanical properties, and the corrosion performance in simulated body fluid (SBF) are presented and compared with reference materials. Furthermore, the successful fabrication of stent prototypes made of the novel alloy and a first functionality test are shown.

2. Experimental Section

2.1. Sample Preparation, Chemical Element Analysis, and Density Measurement

The spherical powders used for the SLM process were prepared by electrode-induction melting gas atomization (EIGA, gas: Ar; TLS Technik, Germany) of cast rods prepared at Leibniz IFW Dresden with a nominal composition of Fe–30Mn–1C–0.025S. The nominal powder particle size was 15–45 μm (mean particle size of 33 μm) and the powder particles showed a high sphericity and a smooth surface with a few satellites.

The Mn and Fe contents of the powder as well as of the SLM-processed samples, designated as FeMnCS (SLM) were checked by inductively coupled plasma optical emission spectrometry (ICP-OES; iCAP 6500 Duo View, Thermo Fisher Scientific). Carrier gas hot extraction (CGHE; EMIA 820V, Horiba) was applied to analyze C and S contents of the samples.

After the EIGA process, a slightly reduced S content compared with the cast starting material was detected in the powder sample (compare **Table 1**) despite working with overpressure. However, the determined chemical compositions of the powder and the FeMnCS (SLM) samples corresponded quite well considering the error limits, as shown in **Table 1**.

As reference material, an austenitic AISI 316L stainless steel (Viray) was used in addition to a cast counterpart with nominal composition of Fe–30Mn–1C–0.25S,^[11] designated as FeMnCS (cast).

The manufacturing of the FeMnCS (SLM) bulk samples and delicate stent structures was conducted with a SLM 250HL device (SLM Solutions) equipped with a 400 W Yb:YAG laser (spot size 80 μm), whereby the processing chamber of the device was flooded with Ar. The layer thickness was set to 30 μm to obtain high geometrical resolution in building direction. For the production of bulk test samples, an energy input of 92 J mm^{−3} was used.

To produce the stent geometries with 2 mm in diameter, a point exposure strategy was used which achieves thin and round struts. The exposure time thereby needs to be of a sufficient duration to allow the melt droplet to connect with the underlying rod. Too long exposure times lead to overly thick rods and too short

exposure times to incomplete connections between the melt pool and the underlying stent rod. In this study, each point was built with 100 W laser power and an exposure time of 400 μs .

The Archimedes method (YDK–01 (0D), Sartorius) was applied for density measurement. For bulk samples, a relative density of 99.6% was achieved, whereas no cracks and minimal distortion could be observed.

2.2. Microstructural Analysis

Microstructural characteristics were investigated by scanning electron microscopy (SEM; Leo 1530 Gemini, Zeiss) combined with energy-dispersive X-ray spectroscopy (EDX; Xflash4010, Bruker) and electron backscatter diffraction (EBSD; e-Flash^{HR}, Bruker). For grain-size determination at least three EBSD measurements per sample were conducted. The software Esprit 2.1 (Bruker) was used for data analysis, and a minimum grain boundary threshold of 15° was chosen.

The samples used for the SEM overview and EDX analysis were first ground to P4000 SiC grit paper and subsequently fine polished up to 0.25 μm diamond and finally polished with Mastermet 2 (Buehler). For the final polishing step of the EBSD samples, OP-S (Struers) was used.

For phase analysis, X-ray diffraction (XRD; Stadi P, STOE, Mo K α 1 radiation) was conducted on ground samples with a thickness of \approx 80 μm in transmission mode.

2.3. Mechanical Characterization

Quasi-static room-temperature compression and tensile tests were conducted at a strain rate of 10^{−3} s^{−1} using a universal testing machine (Instron 8562). The tensile and compression test samples were prepared out of rods, which were built with an orientation of 90° to the substrate plate. Cylindrical samples (3 mm in diameter, 6 mm in length) were used for the compression tests and for the tensile tests, round samples (width of grip section: 4 mm, inner width: 2 mm, gage length: 10 mm, total length: 40 mm) according to DIN 50125:2016-12 were applied. Respectively, three samples were tested under tensile and compressive load.

2.4. Corrosion Tests

The corrosion behavior of SLM and cast FeMnCS bulk samples as well as 316L reference steel was investigated by means of potentiodynamic polarization measurements and by immersion tests in SBF solution at 37 \pm 1 °C according to Kokubo and Takadama^[30] (**Table 2**).

For the potentiodynamic polarization measurements, alloy disc samples with 7 mm diameter and 5 mm thickness were embedded in epoxy resin, ground to P4000 SiC grit, and

Table 1. Chemical composition of the Fe–30Mn–1C–0.02S powder and alloy in wt% determined by ICP-OES and carrier gas hot extraction.

	Fe	Mn	C	S
FeMnCS [powder]	67.71 \pm 0.12	30.85 \pm 0.05	0.974 \pm 0.005	0.0157 \pm 0.0004
FeMnCS [bulk; SLM]	67.90 \pm 0.18	30.26 \pm 0.08	0.991 \pm 0.007	0.0159 \pm 0.0001

Table 2. Chemical composition of the applied SBF.

Species	Na ⁺	K ⁺	Mg ²⁺	Ca ²⁺	Cl [−]	HCO ₃ [−]	HPO ₄ ^{2−}	SO ₄ ^{2−}
Concentration [mmol L ^{−1}]	142	5	1.5	2.5	148.6	4.2	1.0	0.5

ultrasonically cleaned with absolute ethanol. The exposed electrode area was in SLM building direction. The electrochemical tests were conducted in a three-electrode cell connected to a potentiostat (Solartron SI-1287 Electrochemical Interface). The samples served as the rotating disc working electrode (500 rpm), a saturated calomel electrode (SCE) as reference electrode ($E(\text{SHE}) = 0.241 \text{ V}$), and a Pt net as counter electrode. After stabilizing the open-circuit potential (OCP) for 1 h, a potentiodynamic measurement was carried out starting from -0.15 V versus OCP to 1.5 V versus SCE using a scan rate of 0.5 mV s^{-1} . For each material, the measurement was repeated 3–5 times to evaluate the reproducibility of the recorded data.

For immersion testing, samples with a diameter of 10 mm and a thickness of about 1.5 mm were prepared by SLM and ground to P4000 SiC grit as well as ultrasonically cleaned with absolute ethanol. The tests were conducted for two different durations (3 and 7 days) in 450 mL SBF under static conditions. Afterward, the samples were investigated by SEM in combination with EDX to study the corrosion products.

2.5. Balloon Expansion Test

For a first functionality test, FeMnCS stent prototypes with a diameter of 2 mm were processed by SLM, whereby a stent design was chosen, which has the advantage that no support structure was needed for the building process. The expansion abilities of the manufactured stent structures were evaluated with a balloon catheter (Biotronik) connected to a manual pump (B. Braun Melsungen). The change in the stent structure was observed by a digital microscope (VHX 6000, Keyence).

3. Results and Discussion

3.1. Microstructural Properties

In **Figure 1a**, a representative XRD pattern of SLM-processed Fe-30Mn-1C-0.02S bulk material is shown where the alloy consists of face-centered cubic austenite. Further, a fine cellular structure (**Figure 1b**) with a cell width of about 1–2 μm could

be detected in the austenite grain, which is caused by rapid solidification during the SLM process.

In **Figure 2a,b**, the typical microstructure of Fe-30Mn-1C-0.02S obtained via SLM is presented in terms of EBSD mappings of the longitudinal and the cross section. The high cooling rates ($\approx 10^5 \text{ K s}^{-1}$) and corresponding solidification conditions that arise during the SLM process lead to a clear difference in size and morphology of the austenite grains in comparison with those of the cast reference, for which solidification rates of about 10 K s^{-1} can be estimated (**Figure 2c**).^[11,31] Columnar grains which are elongated along the building direction (**Figure 2a**) developed during SLM due to the directional heat flow toward the building plate. The mean grain size (equivalent circular diameter) of the austenite is significantly reduced from $305 \pm 33 \mu\text{m}$ for the cast reference with nearly equiaxed grains to $88 \pm 2 \mu\text{m}$ and $47 \pm 5 \mu\text{m}$ for the longitudinal section and the cross section of an SLM sample, respectively.

The EDX mappings of a FeMnCS (SLM) sample (**Figure 1c–e**) indicate a mostly homogenous distribution of Fe, Mn, S, and C (not shown here). In contrast, the cast reference samples showed a significant enrichment of Mn and a depletion of Fe along the grain boundaries, as shown in **Figure 2e,f** and in previous studies.^[14] Furthermore, fine Mn-rich sulfides were identified mainly along the grain boundaries (compare **Figure 2d,f,g**), that could be indexed by EBSD based on a structure model for $(\text{Fe}_{0.3}\text{Mn}_{0.7})\text{S}$ (space group Fm-3m) (**Figure 2d**).^[32] These precipitates were not detected in the SLM samples. Their formation might be suppressed by the high solidification rates during processing.

3.2. Mechanical Behavior of Bulk Samples under Quasistatic Loading Conditions

These changes in the microstructure have a significant influence on the material properties. In **Figure 3a**, a representative engineering tensile stress–strain curve of FeMnCS (SLM) is presented in comparison with its cast counterpart. The longitudinal axis of the SLM tensile test sample was thereby in the building direction. Characteristic values derived from tensile and compression tests are shown together with those for 316L reference steel in **Table 3**.

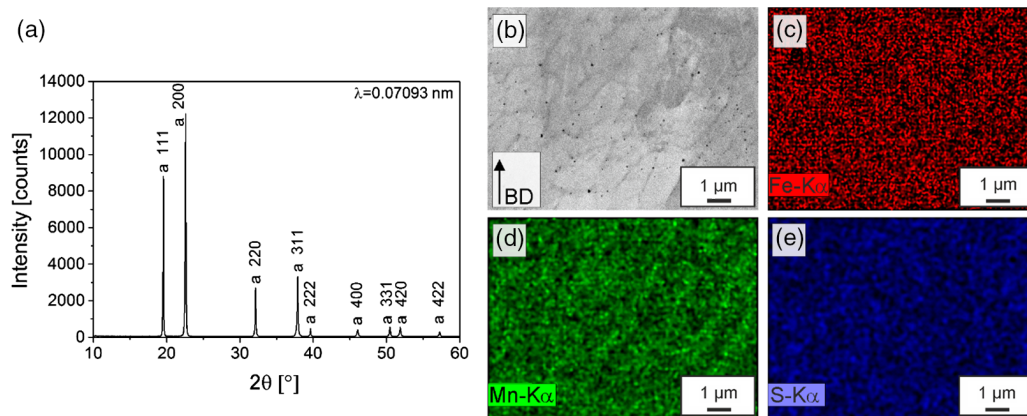


Figure 1. a) XRD pattern of a SLM-processed FeMnCS bulk sample with indexed austenitic “a” phase; b) SEM image of FeMnCS (SLM) with marked building direction (BD) and related EDX mappings of c) Fe, d) Mn, and e) S.

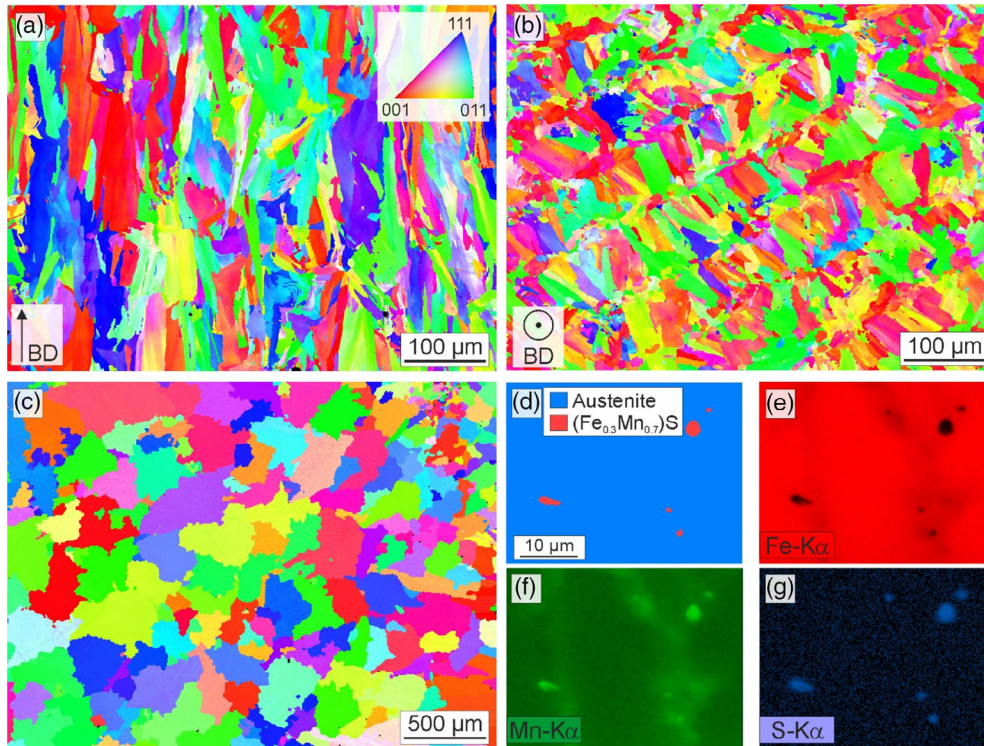


Figure 2. EBSD IPF mapping (color coding with respect to the sample surface) of SLM-processed FeMnCS a) along building direction and b) perpendicular to building direction as well as c) of cast FeMnCS; d) EBSD phase mapping of cast FeMnCS and related EDX mappings of e) Fe, f) Mn, and g) S.

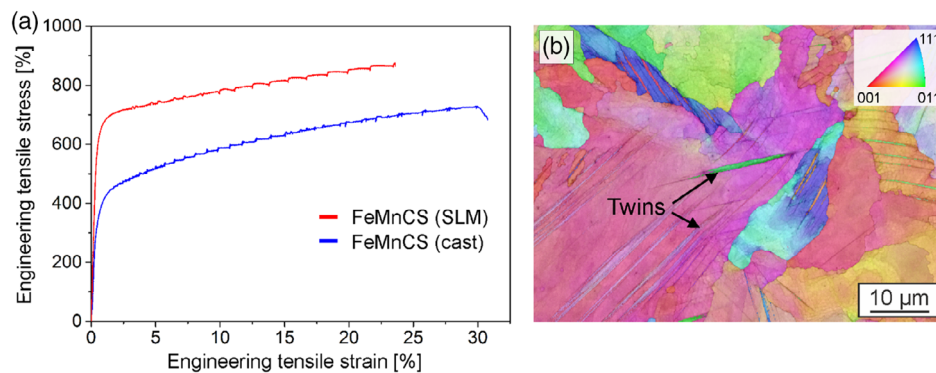


Figure 3. a) Engineering tensile stress–strain curves of SLM-processed FeMnCS and cast reference sample. b) EBSD IPF mapping of FeMnCS (SLM) after 20% of deformation under tensile load (color coding with respect to the sample surface).

Obviously, the sample processed by SLM shows a significantly higher yield strength and ultimate tensile strength, whereby the total tensile strain is slightly reduced compared with the cast reference state (Figure 3a and Table 3). One reason for the decrease in the strain can be higher residual stresses in the SLM sample caused by the more rapid cooling and the high temperature gradient during the process. In addition, both FeMnCS alloy modifications possess (in addition to a good formability) a higher yield and ultimate tensile strength compared with most other degradable Fe-based or Mg-based systems^[8] or a 316L reference steel in the wrought and annealed state (Table 3),^[33] which is considered as the benchmark for novel developed systems.

Furthermore, a higher ultimate tensile strength can be obtained for the FeMnCS (SLM) alloy in comparison with an austenitic SLM-processed 316L steel, whereby the average tensile yield strength and total elongation are slightly lower, but within the range of the standard deviation (Table 3).

The engineering tensile stress–strain curves of the cast and SLM-processed samples shown in Figure 3a show step-like discontinuities in the plastic region which indicate twinning, as it was reported for other FeMnC-based alloys with high Mn contents.^[35,36] Figure 3b shows an example of an SLM-processed sample after a defined tensile deformation of 20%. Deformation twins are exemplarily marked in Figure 3b and identified as $\Sigma 3$

Table 3. Mechanical properties of SLM-processed and cast FeMnCS as well as 316L reference steel.

	FeMnCS [SLM]	FeMnCS [cast]	316L [SLM]	316L [wrought, annealed]
Tensile yield strength, 0.2% offset [MPa]	599 ± 27	341 ± 6 ^[11]	638 ± 22 ^[25]	190 ^[33]
Ultimate tensile strength [MPa]	843 ± 23	767 ± 51 ^[11]	674 ± 9 ^[25]	490 ^[33]
Total elongation [%]	24 ± 4	30 ± 1 ^[11]	30 ± 3 ^[25]	40 ^[33]
Compressive yield strength, 0.2% offset [MPa]	676 ± 37	335 ± 4	200 ^[34]	–
Ultimate compressive strength [MPa]	–	–	650 ^[34]	–
Compressive strain at maximum load [%]	–	–	35 ^[34]	–

twins. The twin boundaries can act as strong barriers to dislocation movement, resulting in a strengthening effect.

So, the combination of high strength and ductility can be also traced back to a twinning-induced plasticity (TWIP) effect, which was already shown for the cast Fe–30Mn–1C–0.025S alloy in previous studies.^[11]

Fracture surface analysis of the vertically built tensile test samples was conducted by SEM, and representative images are shown in **Figure 4**. The fractographs clearly indicate ductile dimple fractures, with small, mainly equiaxed dimples exhibiting diameters up to below 1 μm (Figure 4a,b). Furthermore, small regions of brittle fractures can be observed, as shown in Figure 4a. In addition, several defects like pores or partially molten particles were detected on the fracture surfaces (not shown here), which can induce local stress concentrations and may lead to crack initiation and premature failure, as reported by other authors for SLM-processed 316L steel.^[37]

In addition to the tensile tests, compression tests were conducted, and in **Figure 5**, a representative engineering compressive stress–strain curve of FeMnCS (SLM) is presented in comparison with its cast counterpart. As shown in Table 3, the FeMnCS (SLM) samples (with longitudinal axis parallel to the building direction) show a significantly increased compressive yield strength compared with the as-cast state (Figure 5) and literature values for 316L prepared via SLM.^[34] Furthermore, the material is very ductile, so the compression tests were stopped at a compressive strain of 50% without failure of the samples. Due to a bulging of the sample after ≈15%, the uniaxial stress state changed into a multiaxial stress state, so that the measured values are not representative anymore and, therefore, not shown here.

The enhanced yield strength under tensile and compressive load of FeMnCS (SLM) in comparison with the as-cast state can be mainly attributed to the significantly refined microstructure and accompanying higher fraction of cell and grain boundaries. The cell and grain boundaries thereby act as pinning points, impeding further dislocation propagation, and in turn, strengthen the material.^[38,39]

3.3. Corrosion Testing of Bulk Samples in SBF

In first tests, the corrosion behavior of the considered materials was comparatively assessed under conditions of a SBF. In **Figure 6a**, representative potentiodynamic polarization curves of FeMnCS (SLM), the cast counterpart, and the 316L reference steel measured in SBF under quasi-laminar flow control at 37 °C are presented. For the FeMnCS alloy modifications, generally, a strong active dissolution tendency can be observed, whereby the 316L steel shows a polarization behavior which is typical for a corrosion-resistant material with an anodic passivity plateau before passivity breakdown, and pitting occurs at $E_{\text{anodic}} \approx -0.15$ V versus SCE. The active FeMnCS alloy modifications have much more negative corrosion potentials than 316L steel with $E_{\text{corr}} = -0.32$ V versus SCE. The slightly more positive value for FeMnCS (SLM) of $E_{\text{corr}} = -0.59$ V versus SCE in comparison with that of FeMnCS (cast) of $E_{\text{corr}} = -0.65$ V versus SCE can be attributed to the more homogeneous distribution of the most reactive constituent Mn in the microstructure. The same holds for the corresponding lower corrosion current density of the SLM state of $i_{\text{corr}} = 3.6 \pm 0.3 \mu\text{A cm}^{-2}$ in comparison with that of the as-cast state with $i_{\text{corr}} = 9.6 \pm 0.2 \mu\text{A cm}^{-2}$. Consequently, a lower corrosion rate of $0.82 \pm 0.07 \text{ g m}^{-2} \text{ d}^{-1}$ for the SLM-processed state in

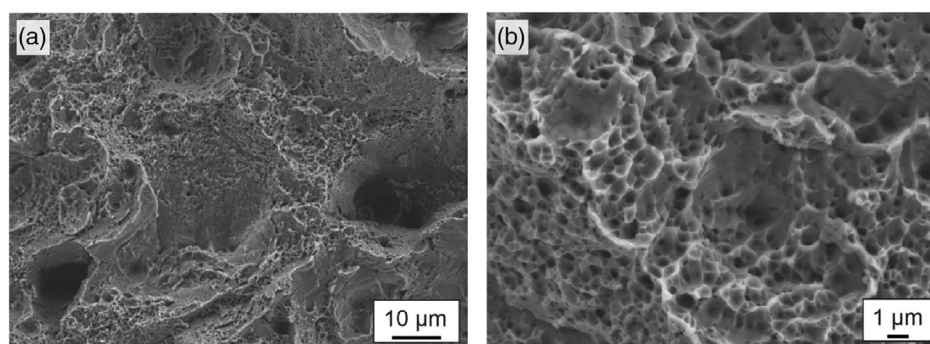


Figure 4. SEM fractographs of vertical built FeMnCS (SLM) tensile test samples: a) overview and b) ductile dimple fracture.

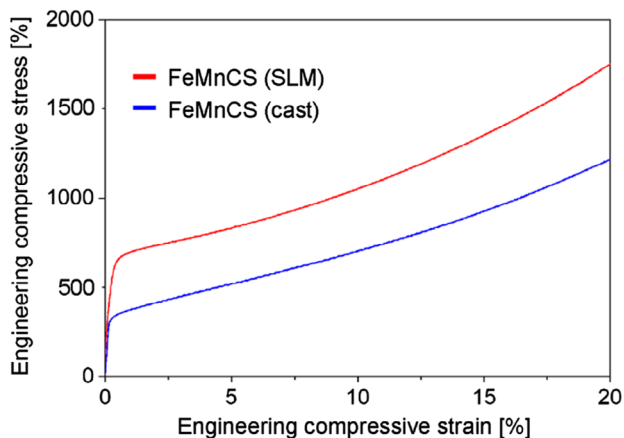


Figure 5. Engineering compressive stress–strain curves of SLM-fabricated FeMnCS and cast reference.

comparison with the as-cast state with $2.42 \pm 0.03 \text{ g m}^{-2} \text{ d}^{-1}$ was determined according to ASTM G102-89(2015).^[40]

In the result of static immersion tests, also conducted in SBF at 37°C , a basically uniform corrosion mode of the SLM samples is revealed, which is desired for maintaining the structural integrity of potential implants also in the degradation period. This can be mainly attributed to the fine-grained single-phase microstructure with homogeneous element distribution (Figure 1b–e).^[41] Localized corrosion phenomena could be only observed around small surface defects, like pores or fine cracks, in the examined SLM samples. In Figure 6b, a SEM image of a FeMnCS (SLM) sample surface after 7 days of static immersion in SBF is shown with a relatively homogenous layer of corrosion products. According to EDX studies (Figure 6c–f), by revealing a high

concentration of Ca, P, and O in the layer as well as to previous X-ray photoelectron spectroscopy (XPS) studies of cast Fe–30Mn–1C–0.025S surfaces^[11,42] and further investigations of FeMn-based alloys immersed in pseudo-physiological solutions,^[8,10] the formation of hydroxyapatite can be assumed. Also, salt precipitations and the formation of oxides are quite probable.^[7,10,11,42]

In contrast to SLM-processed FeMnCS, the cast dual-phase FeMnCS alloy shows a combination of uniform and localized corrosion, leading to a stronger corrosive attack, whereby the analysis of the fundamental corrosion process was presented in previous studies.^[11,42] This can be attributed to the enrichment of the most reactive Mn and depletion of Fe along the austenite grain boundaries, which promote the corrosion attack along these areas. Furthermore, finely distributed manganese sulfide precipitates in the cast modification (Figure 2d) dissolve preferentially in SBF and are initiation sites for pitting corrosion.^[11,43] So, the effect of a microgalvanic couple between different phases plays an important role in the cast modification in comparison with the single-phase SLM-processed state. This active role of manganese sulfide inclusions in steels in the initiation stages of pitting was already presented by several authors.^[44–47]

3.4. Functionality Test of FeMnCS Stent Produced by SLM

To demonstrate the application potential of the novel Fe–30Mn–1C–0.025S alloy, stent prototypes with different diameters down to 1 mm were successfully built by SLM. In Figure 7a–c, microblasted stents with a diameter of 2 mm are presented, whereby a uniform strut thickness of around $120 \mu\text{m}$ could be realized. It was shown that the SLM stents can be successfully expanded with a conventional balloon catheter connected to a manual

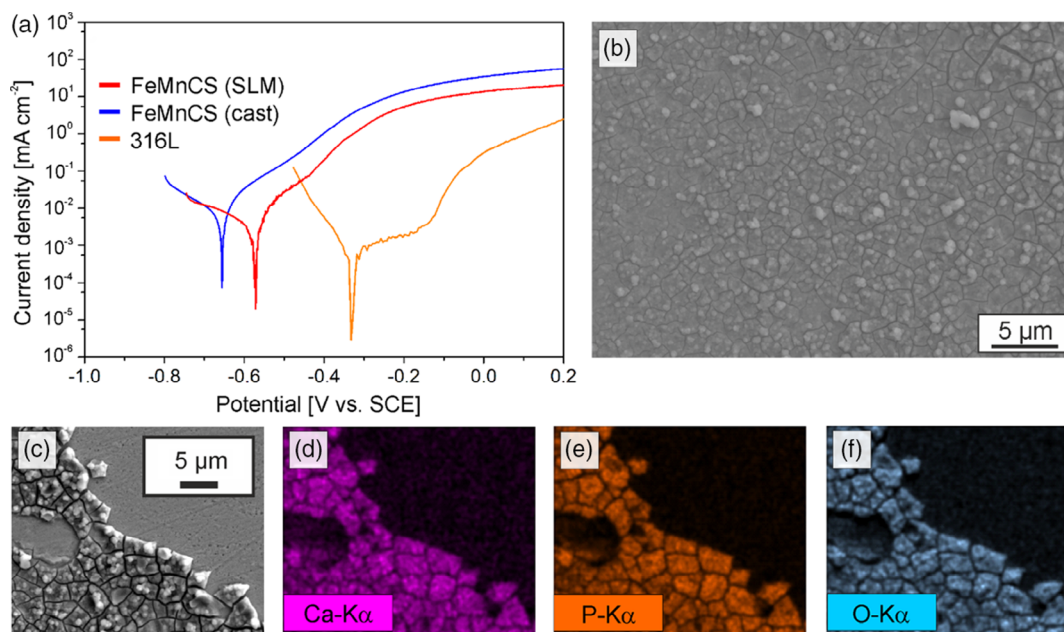


Figure 6. a) Representative potentiodynamic polarization curves of SLM-processed and cast FeMnCS as well as 316L measured in SBF at 37°C ; SEM image of FeMnCS (SLM) b) after 7 days and c) after 3 days of static immersion in SBF at 37°C with related EDX mappings of d) Ca, e) P, and f) O.

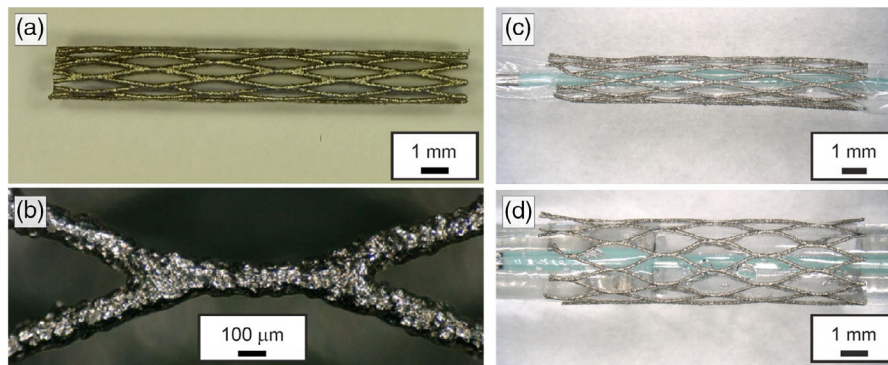


Figure 7. Lightmicrographs of a) a SLM-processed FeMnCS stent and b) stent struts with higher magnification as well as FeMnCS stent (SLM) crimped over a balloon catheter c) before and d) after expansion.

pump delivering water for inflating the balloon, as shown in Figure 7c,d. After applying a pressure of 4.05 bar, the stent had an inner diameter of 3.31 mm (Figure 7d). The stent sprung back to an inner diameter of 2.9 mm after releasing the pressure. To realize a higher grade of deformation in radial direction, optimized additively producible stent geometries are under preparation and will be presented in later studies as well as investigations regarding the influence of the performed deformation on the resulting properties of these structures.

4. Conclusions

In summary, this work demonstrates the successful processing of a novel designed biodegradable Fe–30Mn–1C–0.02S alloy by SLM and the resulting superior properties. When applying this fast solidification technique, austenitic grains with a fine cellular structure and a homogeneous constituent distribution were obtained, resulting in high yield strengths under tensile and compressive load and a very good formability. The novel material exhibits a high ultimate tensile strength of 843 ± 23 MPa in combination with a total elongation of $24 \pm 4\%$ and a compressive yield strength of 676 ± 37 MPa. These strength values for the SLM-processed alloy are significantly higher than those of the cast FeMnCS modification and of a 316L reference steel. The observed combination of high strength and good formability is attributed to the TWIP effect detected by EBSD investigations.

In addition, the SLM samples revealed a reduced corrosion activity in SBF in comparison with that of their cast counterparts which corresponds to an anticipated more uniform degradation mode. Altogether, SLM processing of this novel biodegradable FeMn-based alloy is very promising not only for adjusting beneficial properties, but also for an efficient manufacturing of complex implant structures.

Acknowledgements

The authors would like to thank R. Keller for the sample preparation, H. Bußkamp for conducting the carrier gas hot extraction analysis, and N. Geißler for conducting the mechanical tests. This work was funded by the German Research Foundation (DFG) under grant no. HU 2371/1-1 and project no. 277470500.

Conflict of Interest

The authors declare no conflict of interest.

Keywords

corrosion behaviors, Fe-based alloys, mechanical properties, microstructures, selective laser melting

Received: February 14, 2020

Revised: March 27, 2020

Published online: April 29, 2020

- [1] C. Shuai, L. Liu, M. Zhao, P. Feng, Y. Yang, W. Guo, C. Gao, F. Yuan, *J. Mater. Sci. Technol.* **2018**, *34*, 1944.
- [2] M. Montani, A. Demir, E. Mostaed, M. Vedani, B. Previtali, *Rapid Prototyp. J.* **2017**, *23*, 514.
- [3] T. Niendorf, F. Brenne, P. Hoyer, D. Schwarze, M. Schaper, R. Grothe, M. Wiesener, G. Grundmeier, H. J. Maier, *Metall. Mater. Trans. A* **2015**, *46*, 2829.
- [4] T. Long, X. Zhang, Q. Huang, L. Liu, Y. Liu, J. Ren, Y. Yin, D. Wu, H. Wu, *Virtual Phys. Prototyp.* **2018**, *13*, 71.
- [5] M. Wolff, T. Mesterknecht, A. Bals, T. Ebel, R. Willumeit-Römer, in *Magnesium Technology 2019* (Eds: V. Joshi, J. Jordon, D. Orlov, N. Neelameggham), Springer, Cham **2019**.
- [6] F. Witte, A. Eliezer, in *Degradation of Implant Materials* (Eds: N. Eliaz), Springer, New York, NY, **2012**.
- [7] H. Hermawan, in *Biodegradable Metals: From Concept to Applications*, Springer-Verlag, Heidelberg **2012**.
- [8] Y. Zheng, X. Gu, F. Witte, *Mater. Sci. Eng. R* **2014**, *77*, 1.
- [9] A. Francis, Y. Yang, S. Virtanen, A. R. Boccaccini, *J. Mater. Sci. Mater. Med.* **2015**, *26*, 138.
- [10] H. Hermawan, A. Purnama, D. Dubé, J. Couet, D. Mantovani, *Acta Biomater.* **2010**, *6*, 1852.
- [11] J. Hufenbach, F. Kochta, H. Wendrock, A. Voß, L. Giebeler, S. Oswald, S. Pilz, U. Kühn, A. Lode, M. Gelinsky, A. Gebert, *Mater. Des.* **2018**, *142*, 22.
- [12] E. Mouzou, C. Paternoster, R. Tolouei, A. Purnama, P. Chevallier, D. Dubé, F. Prima, D. Mantovani, *Mater. Sci. Eng. C* **2016**, *61*, 564.
- [13] W. Xu, X. Lu, L. Tan, K. Yang, *Acta Metall. Sin.* **2011**, *47*, 1342.
- [14] J. Hufenbach, H. Wendrock, F. Kochta, U. Kühn, A. Gebert, *Mater. Lett.* **2017**, *186*, 330.

- [15] S. Loffredo, C. Paternoster, N. Giguère, G. Barucca, M. Vedani, D. Mantovani, *Acta Biomater.* **2019**, *98*, 103.
- [16] M. Schinhammer, A. C. Hänzli, J. F. Löffler, P. J. Uggowitzer, *Acta Biomater.* **2010**, *6*, 1705.
- [17] P. Wen, L. Jauer, M. Voshage, Y. Chen, R. Poprawe, J. H. Schleifenbaum, *J. Mater. Process. Technol.* **2018**, *258*, 128.
- [18] D. Carluccio, A. G. Demir, L. Caprio, B. Previtali, M. J. Bermingham, M. S. Dargusch, *J. Manuf. Process.* **2019**, *40*, 113.
- [19] Bär, L. Berger, L. Jauer, G. Kurtuldu, R. Schäublin, J. H. Schleifenbaum, J. F. Löffler, *Acta Biomater.* **2019**, *98*, 36.
- [20] M. Wiesener, K. Peters, A. Taube, A. Keller, K.-P. Hoyer, T. Niendorf, G. Grundmeier, *Mater. Corr.* **2017**, *9999*, 1.
- [21] J. O. Milewski, *Additive Manufacturing of Metals: From Fundamental Technology to Rocket Nozzles, Medical Implants, and Custom Jewelry*, Springer International Publishing, Cham **2017**.
- [22] C. Y. Yap, C. K. Chua, Z. L. Dong, Z. H. Liu, D. Q. Zhang, L. E. Loh, S. L. Sing, *Appl. Phys. Rev.* **2015**, *2*, 041101.
- [23] L.-C. Zhang, H. Attar, *Adv. Eng. Mater.* **2016**, *18*, 463.
- [24] E. Chlebus, B. Kuźnicka, T. Kurzynowski, B. Dybala, *Mater. Charact.* **2011**, *62*, 488.
- [25] I. Tolosa, F. Garciandía, F. Zubiri, F. Zapirain, A. Esnaola, F. Zapirain, *Int. J. Adv. Manuf. Technol.* **2010**, *51*, 639.
- [26] A. Takaichi, A. Suyalatu, T. Nakamoto, N. Joko, N. Nomura, Y. Tsutsumi, S. Migita, H. Doi, S. Kurosu, A. Chiba, N. Wakabayashi, Y. Igarashi, T. Hanawa, *J. Mech. Beh. Biomed. Mater.* **2013**, *21*, 67.
- [27] Y. J. Liu, Y. S. Zhang, L. C. Zhang, *Materialia* **2019**, *6*, 100299.
- [28] L. C. Zhang, D. Klemm, J. Eckert, Y. L. Hao, T. B. Sercombe, *Scripta Mater.* **2011**, *65*, 21.
- [29] N. Dai, L.-C. Zhang, J. Zhang, X. Zhang, Q. Ni, Y. Chen, M. Wu, C. Yang, *Corros. Sci.* **2016**, *111*, 703.
- [30] T. Kokubo, H. Takadama, *Biomater.* **2006**, *27*, 2907.
- [31] J. Sander, J. Hufenbach, M. Bleckmann, L. Giebeler, H. Wendrock, S. Oswald, T. Gemming, J. Eckert, U. Kühn, *J. Mater. Sci.* **2017**, *52*, 4944.
- [32] G. Loseva, L. Ryabinkina, A. Smyk, *Solid St. Phys.* **1986**, *28*, 596.
- [33] ASTM F138-13a, *Standard Specification for Wrought 18 Chromium-14 Nickel-2.5 Molybdenum Stainless Steel Bar and Wire for Surgical Implants*, ASTM International, West Conshohocken, PA **2013**.
- [34] S. Dadbakhsh, L. Hao, N. Sewell, *Rapid Prototyp. J.* **2012**, *18*, 241.
- [35] O. Bouaziz, S. Allain, C. Scott, P. Cugy, D. Barbier, *Curr. Opin. Solid St. Mater Sci.* **2011**, *15*, 141.
- [36] H. Idrissi, K. Renard, L. Ryelandt, D. Schryvers, P. J. Jacques, *Acta Mater* **2010**, *58*, 2464.
- [37] R. Casati, J. Lemke, M. Vedani, *J. Mater. Sci. Technol.* **2016**, *32*, 738.
- [38] N. Hansen, *Scr. Mater.* **2004**, *51*, 801.
- [39] C. Qiu, M. Al Kindi, A. Salim Aladawi, I. Al Hatmi, *Sci. Rep.* **2018**, *8*, 7785.
- [40] ASTM G102-89(2015)e1, *Standard Practice for Calculation of Corrosion Rates and Related Information from Electrochemical Measurements*, ASTM International, West Conshohocken, PA **2015**.
- [41] P. Qin, Y. Chen, Y.-J. Liu, J. Zhang, L.-Y. Chen, Y. Li, X. Zhang, C. Cao, H. Sun, L.-C. Zhang, *ACS Biomater. Sci. Eng.* **2019**, *5*, 1141.
- [42] A. Gebert, F. Kochta, A. Voß, S. Oswald, M. Fernandez-Barcia, U. Kühn, J. Hufenbach, *Mater. Corr.* **2018**, *69*, 167.
- [43] A. Pardo, M. Merino, A. Coy, F. Viejo, R. Arrabal, E. Matykina, *Corros. Sci.* **2008**, *50*, 1796.
- [44] P. Schmuki, H. Hildebrand, A. Friedrich, S. Virtanen, *Corr. Sci.* **2005**, *47*, 1239.
- [45] J. Stewart, D. Williams, *Corr. Sci.* **1992**, *33*, 457.
- [46] B. Vuillemin, X. Philippe, R. Oltra, V. Vignal, L. Coudreuse, L. Dufour, E. Finot, *Corr. Sci.* **2003**, *45*, 1143.
- [47] E. G. Webb, R. C. Alkire, *J. Electrochem. Soc.* **2002**, *149*, B272.